BAYESIAN RECONSTRUCTION IN EMISSION COMPUTERIZED TOMOGRAPHY

Z. Liang and H. Hart

Department of Nuclear Medicine, Montefiore Medical Center, Bronx, NY 10467;
Department of Physics, City College of New York, New York, NY 10031.

ABSTRACT

Iterative Bayesian image reconstruction algorithms for emission computerized tomography have been derived and applied using three general classes of a priori source distribution constraints: 1) maximum entropy constraints on source elements; 2) source continuity and boundary information; 3) ideal and fuzzy pattern source distribution constraints. This work has recently been extended to include a combined Bernoulli process and entropy analysis on source element strength correlations and also to provide for more general a priori probability distributions of probable source element strengths in sub-sets of a source field. Improvement in image reconstruction over standard methods has been demonstrated by applying these Bayesian algorithms to computer simulation data and experimental nuclear isotope imaging data.

INTRODUCTION

Incorporating a priori source information in Bayesian formalism for image reconstruction has recently attracted more attention [1-3]. We have proposed a Bayesian image processing (BIP) formalism and derived iterative BIP algorithms using several different classes of a priori source distribution constraints [4-11]. This work has now been extended to include a statistical Bernoulli process of source elements with fixed total number of photon emissions and a maximum entropy analysis on individual source element probability distributions. It has also been extended to provide for more general a priori probability distributions of probable source element strengths in sub-sets. Such a priori source information is formulated in terms of probability density functions of source element strengths and spatial correlations. The corresponding iterative BIP algorithms are derived by maximizing the Bayesian functions via the expectation-maximization technique and assuming data obey Poisson statistics [12-14]. Improved results obtained by applying the algorithms to computer generated data and experimental phantom imaging data are presented.

A PRIORI SOURCE INFORMATION FUNCTIONS

As shown in reference [6], maximum entropy considerations result in a Poisson functional form of probability density function $p_j(\phi_j)$ for each source element (voxel) strength ϕ_j under the assumption of the existance of a defined mean $\bar{\phi}_j$ and a defined variation $\sigma_j^2 (= \bar{\phi}_j)$ for random variable $\phi_j \geq 0$, i.e.,

$$p_j(\phi_j) = e^{-\bar{\phi}_j} \frac{(\bar{\phi}_j)^{\phi_j}}{\phi_j!}. \tag{1}$$

In nuclear isotope imaging applications, function $P_j(\phi_j)$ stands for the a priori probability distribution of the photon emission from voxel j per unit time at time $t = 0$.

If all voxel values $\{\phi_j\} = \Phi$ are uncorrelated with each other, then the a priori probability density function of the source distribution Φ is:

$$P_1(\Phi) = \prod_{j=1}^{J} p_j(\phi_j) = \prod_{j=1}^{J} e^{-\bar{\phi}_j} \frac{(\bar{\phi}_j)^{\phi_j}}{\phi_j!} \tag{2}$$

where J is the number of voxels.

If the total number N of emitted photons is approximately fixed (corresponding hypothetically to a given patient dose and an extended count time), all voxel values are no longer strictly uncorrelated with each other. The distribution of the N photons over the J voxels can then be assumed to obey a Bernoulli process [15], whence:

$$P_2(\Phi) = \frac{N!}{\prod_j \phi_j!} \prod_{j=1}^{J} [\, p_j(\phi_j) / h_j \,]^{\phi_j} \tag{3}$$

where each voxel value has the Poisson functional probability distribution (1) and the sum of $\{\bar{\phi}_j\}$ is proportional to the total number N, $h_l = \sum_j p_j(\phi_j)$ is a normalization constant.

Note that although the two source probability functions $P_1(\Phi)$ and $P_2(\Phi)$ reflect two different physical modeling processes, both of them assume that each voxel value ϕ_j has a defined mean $\bar{\phi}_j$ and a defined variation without knowing their values.

In some cases, a voxel value in an a priori sub-set of source field can be more restrictively characterized by a given probable mean value and variation. It will then have a set of discrete probabilities of falling into each of the discrete gray levels reflecting the intensity resolution of the imaging system. Such a priori probability information of source distributions around a set of probable source strengths can be expressed by the probability density functions (4), (5) and (7) below.

As outlined in reference [7], if the strengths of source elements can be divided into $k+1$ distinct gray levels of $\{\phi_s^e\}$, $s = 0, 1, ..., k-1$, and each voxel value ϕ_j has different probabilities of falling into each of the gray levels, then

$$p_j(\phi_j) = \sum_{s=1}^{K} C_s e^{-\frac{(\phi_j - \phi_s^e)^2}{2\sigma_s^2}} + C_0 e^{-\phi_0^e} \frac{(\phi_0^e)^{\phi_j}}{\phi_j!} \tag{4}$$

where the last term can have a Poisson rather than a Gaussian functional form to exclude negative source strengths for voxels associated with the lowest gray level ϕ_0^e and the C_s and C_0 are the normalization constants reflecting the anticipated average number of voxels falling within corresponding gray levels $\{\phi_s^e\}$ and ϕ_0^e.

If there is no spatial correlation information available, the probability density function of the source distribution is:

$$P_3(\Phi) = \prod_{j=1}^{J} p_j(\phi_j)$$

$$= \prod_{j=1}^{J} [\, \sum_{s}^{K} C_s e^{-\frac{(\phi_j - \phi_s^e)^2}{2\sigma_s^2}} + C_0 e^{-\phi_0^e} \frac{(\phi_0^e)^{\phi_j}}{\phi_j!} \,]. \tag{5}$$

With spatial correlations of source element strengths available, the source distribution can be viewed as a patterned source distribution. Assume as one possibility that the spatial correlation function $w(l)$ has the Gaussian functional form:

$$w(l) = a\, e^{-b\,(l - l_s)^2}, \tag{6}$$

then [8]

$$P_4(\Phi) = \prod_{j=1}^{J} \{\, c \sum_{q} [\, w(l_q) \prod C_s e^{-\frac{(\phi_{j \pm l_{qs}} - \phi_s^e)^2}{2\sigma_s^2}} \,] + C_0 e^{-\phi_0^e} \frac{(\phi_0^e)^{\phi_j}}{\phi_j!} \,\} \tag{7}$$

where a, b and c are constants, index q sums over different probable pattern configurations.

The four a priori source probability information functions $P_1(\Phi)$, $P_2(\Phi)$, $P_3(\Phi)$ and $P_4(\Phi)$ are presented above in the order of from least to most restrictive. They can be applied to

0018-9499/88/0200-0788$01.00

correspondingly suitable situations. Each of these functions will be used to derive the iterative BIP algorithms respectively assuming Poisson statistics in the following section.

ITERATIVE BIP ALGORITHMS

Bayesian image processing offers the potential to yield a maximum likelihood source distribution Φ^* incorporating any a priori source information which may be available. Mathematically, this is expressed by the Bayes' Law:

$$P(\Phi \mid Y) = P(Y \mid \Phi)\ P(\Phi) / P(Y) \tag{8}$$

and Φ^* maximizes the ln Bayesian function $\ln P(\Phi \mid Y)$

$$\frac{\partial}{\partial \phi_k} \ln P(\Phi \mid Y) \mid_{\Phi=\Phi^*} = 0 \tag{9}$$

where the likelihood probability density function $P(Y \mid \Phi)$ reflects the statistical nature of measured data Y from source distribution Φ, the a priori source probability density function $P(\Phi)$ was discussed in the previous section and the data probability density function

$$P(Y) = \int_\Omega P(Y \mid \Phi)\, P(\Phi)\, d\Phi \tag{10}$$

is not related to the maximal value of $P(\Phi \mid Y)$ and so will be omitted.

If there is no a priori source information available, $P(\Phi)$ can be assumed as constant, implying that all possible source distributions are equally likely; maximizing the Bayesian function results in the same solution as maximum likelihood [13-14].

For each data element (or projection ray) obeying Poisson statistics with all of them statistically uncorrelated, the likelihood function $P(Y \mid \Phi)$ has the form:

$$P(Y \mid \Phi) = \prod_{i=1}^{I} e^{-\sum_j R_{ij}\phi_j} \frac{(\sum_j R_{ij}\phi_j)^{Y_i}}{Y_i!} \tag{11}$$

where I is the number of data elements, R_{ij} the probability of photons emitted at voxel j and contributing to data element Y_i, and $\sum_j R_{ij}\phi_j$ the mean of random variable Y_i.

In nuclear medical imaging, R_{ij} include the effects of radioisotope decay, tissue attenuation and scattering and can be determined by scanning a point source (i.e. point spread function). More detail about R_{ij} will be given in the discussion section.

With the a priori source information (2), (3), (5) and (7) available and assuming Poisson statistics (11), the Bayesian solution Φ^* is determined by a system of equations, from Eq.(9),

$$\sum_{i=1}^{I} R_{ik} \left(\frac{Y_i}{\sum_j R_{ij}\phi_j^*}\right) = \sum_i R_{ik} - \frac{\partial}{\partial \phi_k} \ln P(\Phi) \mid_{\Phi=\Phi^*}. \tag{12}$$

The expectation-maximization technique [12-14], among many other iterative schemes [16-17], can be employed to derive iterative BIP algorithms for the solution Φ^*.

The general form of the iterative BIP algorithms is:

$$\phi_k^{(n+1)} = \phi_k^{(n)} \frac{\sum_i R_{ik} \left(Y_i / \sum_j R_{ij}\phi_j^{(n)}\right)}{\sum_i R_{ik} + \xi_k^{(n)} Z_k^{(n)}(\Phi^{(n)})} \tag{13}$$

with

$$Z_k^{(n)}(\Phi^{(n)}) = -\frac{\partial}{\partial \phi_k} \ln P(\Phi) \mid_{\Phi=\Phi^{(n)}+\lambda d^{(n)}} \tag{14}$$

and

$$\xi_k^{(n)} = \frac{A\, n^\kappa}{B + n^\kappa} \sum_i R_{ik} \tag{15}$$

where λ is the step length of the a priori information increase along the direction $\mathbf{d}^{(n)}$ at the n-th iteration, as a simple choice, $\lambda \approx 1$ and $\mathbf{d}^{(n)} = \Phi^{(n)} - \Phi^{(n-1)}$; the role of the adjustable sigmoidal parameter $\xi_k^{(n)}$ is to impose the effect of the a priori constraints $P(\Phi)$ gradually. The parameters A, B and κ are constants.

(a). For the a priori probability density function $P_1(\Phi)$ of source distribution Φ (2),

$$Z_k^{(n)} = \left[\ln\left(\frac{\phi_k}{\bar{\phi}_k}\right) + \frac{1}{2\phi_k}\right] \mid_{\phi_k = \phi_k^{(n)} + \lambda d_k^{(n)}}. \tag{16}$$

(b). Using the a priori information $P_2(\Phi)$ of (3),

$$Z_k^{(n)} = [2\phi_k \ln\left(\frac{\phi_k}{\bar{\phi}_k}\right) + (\bar{\phi}_k - \phi_k) + \frac{3}{2}\ln(\phi_k) + \frac{1}{2\phi_k} + H] \tag{17}$$

where $\phi_k = \phi_k^{(n)} + \lambda d_k^{(n)}$ and H is a constant relating to h_k in (3).

(c). Substituting the a priori source constraint $P_3(\Phi)$ of (5) into Eq.(14),

$$Z_k^{(n)} = \frac{\sum_s C_s [(\phi_k - \phi_s^e)/\sigma_s^2]\, e^{-U_s(\phi_k)} + p_k(\phi_k) X_k}{\sum_s C_s\, e^{-U_s(\phi_k)} + p_k(\phi_k)} \tag{18}$$

where $p_k(\phi_k)$ is the Poisson function (1) with $\bar{\phi}_k = \phi_0^e$, $U_s(\phi_k) = (\phi_k - \phi_s^e)^2 / (2\sigma_s^2)$, and $X_k = \ln(\phi_k / \phi_0^e) + 1/(2\phi_k)$.

(d). Considering the a priori patterned source distribution constraint $P_4(\Phi)$ of (7),

$$Z_k^{(n)} = \frac{c \sum_q Q_k\, w(l_q) \prod_s C_s\, e^{-V_s(\phi_k)} + p_k(\phi_k) X_k}{c \sum_q [w(l_q) \prod_s C_s\, e^{-V_s(\phi_k)}] + p_k(\phi_k)} \tag{19}$$

where $V_s(\phi_k) = (\phi_{k \pm l_{qs}} - \phi_s^e)^2 / (2\sigma_s^2)$, and $Q_k = (\phi_k - \phi_q^e)/\sigma_q^2$.

The four iterative BIP algorithms, expressed by Eqs.(13) and (15) with (16), (17), (18) and (19) respectively, will be applied to computer generated data and experimental phantom imaging data for image reconstruction in the next section.

SIMULATION AND EXPERIMENTAL RESULTS

Computer simulation is carrying out in three steps. First a two dimensional source distribution $\{S_j\}$ is specified, as in Fig.1, with two point sources of strength 109, separated by 8 voxel units, superimposed upon a background of strength 1 source unit. The point spread function PSF is calculated from an assumed functional form:

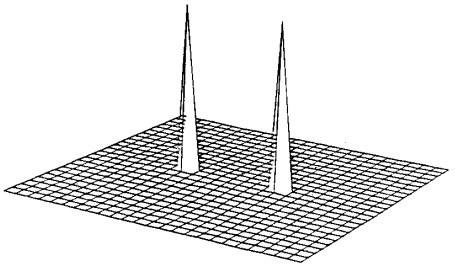

Fig.1: Source distribution consisting of two point sources of strength 109, separated by 8 voxel units, superimposed upon a background of strength 1 unit.

$$R_{ij} \approx e^{-\ln(2)(i-j)^2/T^2} \tag{20}$$

where $T = FWHM/2 = 4$ voxel units, a rather poor resolution imaging system.

Second, the data distribution $\{Y_i\}$ is calculated using the relation

$$Y_i = \sum_{j=1}^{J} R_{ij}\, S_j \tag{21}$$

as shown in Fig.2. Note that here Y_i are ideal data. The effects of Poisson randomization are studied using experimental phantom imaging data.

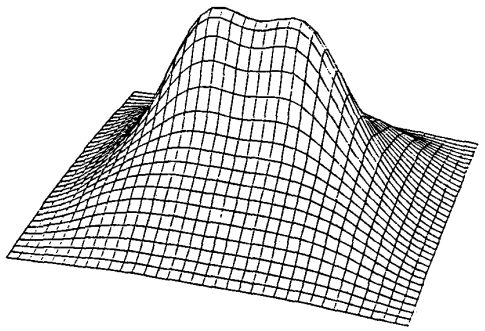

Fig.2: Ideal data distribution calculated using Eq.(21).

The last step is to apply the four algorithms to the simulation data $\{Y_i\}$, where the initial estimate can be assumed, for simplicity, as:

$$\phi_k^{(0)} = Y_k \; / \sum_i R_{ik} \; . \tag{22}$$

Since algorithms (16) and (17) are derived on the assumption of each voxel value ϕ_j having a defined mean $\bar{\phi}_j$, an optimal choice of $\bar{\phi}_j$ is to let $\{\bar{\phi}_j = S_j\}$. Under this condition, algorithms (16) and (17) generate almost identical results to that of Fig.1 in less than 5 iterations.

Since $\{S_j\}$ is of course generally unknown, the choice of $\{\bar{\phi}_j = S_j\}$ is unavailable in most situations. A more realistic very weakly restrictive choice was therefore usually employed:

$$\bar{\phi}_k = \phi_k^{(n+1)} + \tau \, d_k^{(n)} = \phi_k^{(n)} + (\lambda + \tau) \, d_k^{(n)} . \tag{23}$$

If the step factor $\tau = 0$, the mean of voxel k is the update iterated voxel value. In this case, algorithm (16) approachs the ML result [13-14, 6]. With $\tau > 0$, the mean value advances in the direction $d_k^{(n)}$. As usual, $\tau \approx 1$. Figs.3 and 4 show the results of algorithms (16) and (17) respectively after 100 iterations for the simulation data (21), where the constants $A \approx 1.0$, $B = L^{\kappa}$, $\kappa = 2$, and L is the number of iterations.

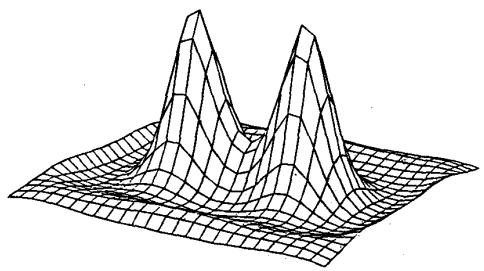

Fig.3: Result using algorithm (16) at 100 iterations on ideal data.

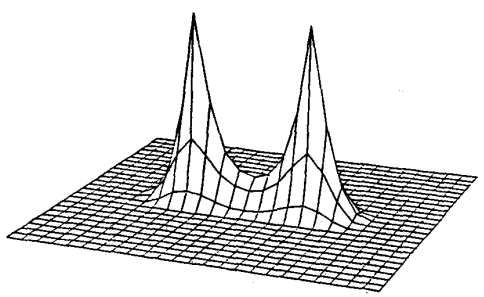

Fig.4: Result using algorithm (17) at 100 iterations on ideal data.

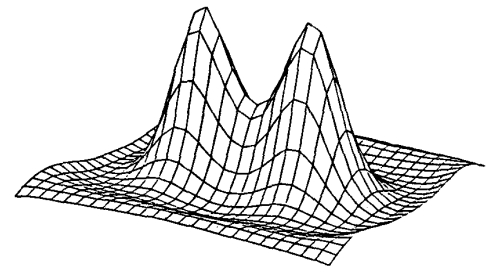

Fig.5: Result using the ML algorithm at 100 iterations on ideal data.

For comparison, the ML algorithm [13-14] (i.e. letting $Z_k^{(n)} = 0$ for Eq.(13)) is applied to the simulation data for 100 iterations and the result is shown in Fig.5.

In carrying out the algorithms (18) and (19), the normalization constants C_s and C_0, and constant c are combined and assumed as having the functional form:

$$\eta^{(n)} = \frac{A_0 \, n^{\kappa}}{B + n^{\kappa}} \tag{24}$$

multiplied by the Poisson terms in (4), (5), (7), (18) and (19) with $A_0 \approx 10.0$. It increases the effect of the background level ϕ_0^c gradually. The estimated probable values $\{\phi_s^c\}$ and ϕ_0^c can be calculated using Eq.(21) with and without the point sources in the background source distribution, using the factor $\sum_{ij} R_{ij}$ [10]. The correct and incorrect values $\phi_0^c = 1.0$, $\phi_1^c = 105$ and $\phi_2^c = 115$ were used for three gray levels. The constants in the spatial correlation function (6) were chosen as $a = 1$, $b = 0.25$ and $l_s = 7$ rather than the correct value of 8 voxel units. The results of algorithms (18) and (19) after 50 iterations for the simulation data are almost identical to that of Fig.1.

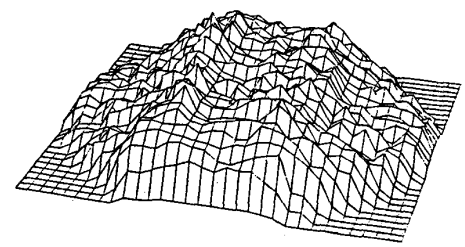

Fig.6: Experimental imaging data from a phantom consisting of two parallel lines of tubing.

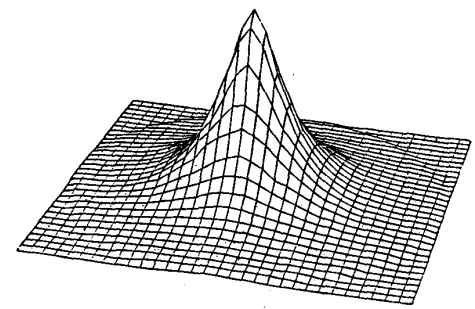

Fig.7: The experimental point source spread function for Co^{57}.

Experimental phantom imaging data were obtained by using a Picker Dyna Gamma Camera without a collimator and imaging two parallel catheters containing a solution Co^{57} in a plane parallel to the camera face. The output from the camera was arranged in a 32x32 matrix as shown in Fig.6 with the two lines of tubing oriented in the y-direction.

The PSF is the camera output imaging a point source of Co^{57} at the same depth as the two lines of tubing and is arranged in a 32x32 matrix as shown in Fig.7. The $FWHM$ = 9 pixel units is very close to the separation of the two lines of tubing. Since the camera system can be assumed to be approximately spatially invariant, R_{ij} is then formed from PSF [18].

The initial estimate $\phi_k^{(0)}$ is calculated using Eq.(22) with the measured $\{Y_i\}$ and $\{R_{ij}\}$.

Figs.8 and 9 are the results of algorithms (16) and (17) respectively after 25 iterations for the phantom imaging data. The ML algorithm generates a result, shown in Fig.10, after 50 iterations.

The estimate values $\phi_0^s = 8$, $\phi_1^s = 105$, $\phi_2^s = 115$ and $l_s = 7$ were used in carrying out the results of algorithms (18) and (19) for the phantom imaging data. Figs.11 and 12 show the results of algorithms (18) and (19) respectively after 25 iterations.

The comparisons of the results of using BIP algorithms and the ML algorithm for the computer simulation and experimental phantom imaging data demonstrate the improvement in image processing if valid a priori source information of (5) and (7) is available or the general source distribution modeling functions (2) and (3) are used.

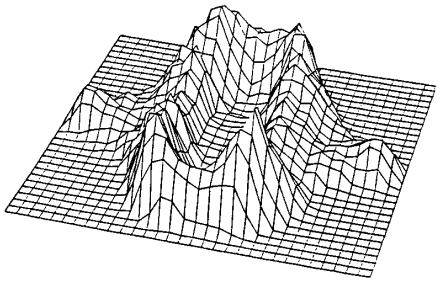

Fig.8: Result using algorithm (16) for 25 iterations on the phantom imaging data.

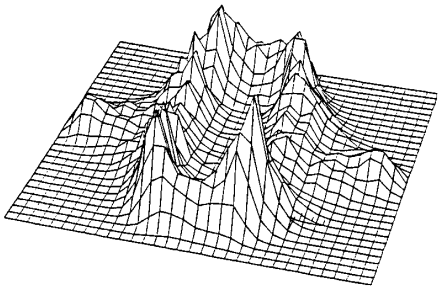

Fig.9: Result using algorithm (17) for 25 iterations on the phantom imaging data.

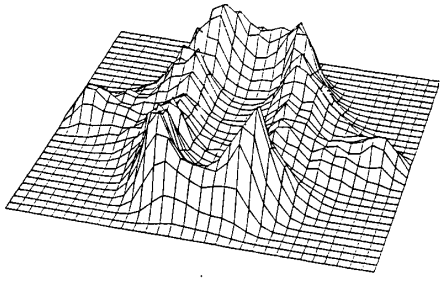

Fig.10: Result using the ML algorithm for 50 iterations on the phantom imaging data.

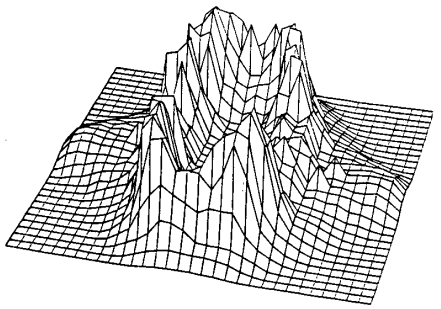

Fig.11: Result using algorithm (18) for 25 itera--tions on the phantom imaging data.

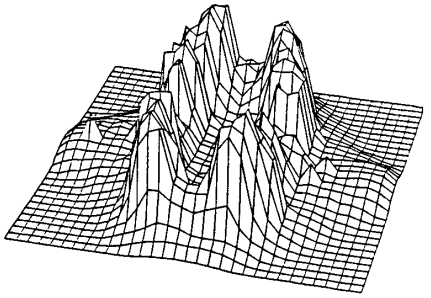

Fig.12: Result using algorithm (19) for 25 itera--tions on the phantom imaging data.

DISCUSSION

The BIP formalism has the advantage of considering both the statistical behavior of the measured data and a priori source distribution information. In this paper and previous work [4-11], we focused on the a priori source element strength and spatial correlation information. In emission computerized tomography, the tissue attenuation and scattering may be also an example of a priori source information. There are two ways to handle the attenuation and scattering correction, one is to incorporate the correction into the values $\{R_{ij}\}$ and another is into the probability density function $P(\Phi)$.

As indicated by function (11) and [6], R_{ij} include the effects of radioisotope decay, tissue attenuation and scattering. Specifically, the effect of radioisotope decay decreases the photon emission gradually as a factor $e^{-\alpha t_i}$ during the scanning period, where α is the decay constant and t_i the time at which the data element Y_i is being measured.

The attenuation effect influences PET and SPECT in different ways [16, 19-20]:

(1). for PET, the attenuation factor is $exp[-\int_0^{L_i} u(l_i)\,dl_i]$, where l_i is the path coordinate of projection ray Y_i, L_i the path length of Y_i intersecting the patient body, and u the absorption coefficient. Since the factor is independent of the voxel index j, so the mean value of Y_i becomes by analogy with prior work [19]:

$$\sum_j R_{ij}\phi_j = exp[-\int_0^{L_i} u(l_i)\,dl_i - \alpha t_i] \sum_j R_{ij}^0 \phi_j \qquad (25)$$

where R_{ij}^0 depends only upon the projection-voxel geometry and scattering. The exponential term of Eq.(25) can be calculated easily prior to image reconstruction for each projection ray Y_i if the absorption coefficient u and body contour are known. Note that the attenuation correction of the mean value of (25) is different from those of the projection value correction [19, 21].

(2). for SPECT, the attenuated mean value of Y_i is:

$$e^{-\alpha l_i} \sum_j R_{ij}^0 \phi_j \exp[-\int_{l_j}^{L_i^0} u(l_i)\, dl_i] \qquad (26)$$

where L_i^0 is the path length of photons from voxel j to the surface of the patient body along projection ray Y_i and l_j is the position of voxel j on Y_i [22-23].

Somewhat more exact means of calculating scattering and attenuation corrections are currently being formulated using the Compton and Rayleigh scattering formulas [24-25]. The work is in progress on incorporating formulas (25), (26), and scattering effect and attenuation correction of $P(\Phi)$ into Bayesian formalism.

REFERENCES

[1] E. Levitan and G. Herman, "A Maximum a Posteriori Probability Expectation Maximization Algorithm for Image Reconstruction in Emission Tomography". IEEE Trans. Med. Imaging, vol.6, 185-192, 1987.

[2] S. Geman and D. McClure, "Statistical Methods for Tomographic Image Reconstruction". Bull. ISI, vol.52, to appear.

[3] G. Herman, H. Hurwitz, A. Lent. and H. Lung, "On the Bayesian Approach to Image Reconstruction". Inf. Control, vol.42, 60-71, 1979.

[4] Z. Liang and H. Hart, "Bayesian Image Processing of Data from Generically Constrained Source Dstributions". J. Biophys., vol.49, 243, 1986.

[5] H. Hart and Z. Liang, "Bayesian Image Processing of Data from Quantitatively Constrained Source Distributions". J. Biophys., vol.49, 243, 1986.

[6] Z. Liang and H. Hart, "Bayesian Image Processing of Data from Constrained Source Distributions, I: non-valued, uncorrelated and correlated constraints". Bull. Math. Biol., vol.49, 51-74, 1987.

[7] H. Hart and Z. Liang, "Bayesian Image Processing of Data from Constrained Source Distributions, II: valued, uncorrelated and correlated constraints". Bull. Math. Biol., vol.49, 75-91, 1987.

[8] Z. Liang and H. Hart, "Bayesian Image Processing of Data from Constrained Source Distributions -- fuzzy pattern constraints". Phys. Med. Biol., to appear.

[9] Z. Liang and H. Hart, "Source Continuity and Boundary Considerations in Bayesian Image Processing". submitted to pubilication.

[10] H. Hart and Z. Liang, "Bayesian Image Processing in Two Dimensions". IEEE Trans. Med. Imaging, vol.6, 201-208, 1987.

[11] Z. Liang and H. Hart, "Boundary Enhancement with a Priori Constraints". ACEMB, vol.29, 214, 1987.

[12] A. Dempster, N. Laird and D. Rubin, "Maximum Likelihood from Incomplete Data via the EM Algorithm". JRSS, vol.39, 1-38, 1977.

[13] L. Shepp and Y. Vardi, "Maximum Likelihood Reconstruction for Emission Tomography". IEEE Trans. Med. Imaging, vol.2, 113-122, 1982.

[14] K. Lange and R. Carson, "EM Reconstruction Algorithms for Emission and Transmission Tomography". JCAT vol.8, 306-316, 1984.

[15] C. Rao, *Advanced Statistical Methods in Biometric Research*. John Wiley & Sons, Inc., NY., 1951.

[16] Z. Liang, Ph.D. Dissertation, City Univ. of New York, 1986.

[17] D. Luenberger, *Linear and Non -linear Programming*. Addison-Wesley, Inc., NY., 1984.

[18] H. Andrews and B. Hunt, *Digital Image Restoration*. Prentice-Hall, Inc., NY., 1977.

[19] S. Huang, E. Hoffman, M. Phelps and D. Kuhl, "Quantitation in PET: 2. Effects of Inaccurate Attenuation Correction". JCAT, vol.3, 804-814, 1979.

[20] T. Walters, W. Simon, . Chesler and J. Correia, "Attenuation Correction in Gamma Emission Computed Tomography". JCAT, vol.5, 89-94, 1981.

[21] M. Phepls, E. Hoffman, N. Mullani and M. Ter-Pogossian, "Application of Annihilation Coincidence Detection to Transaxial Reconstruction Tomography". J. Nucl. Med., vol.16, 210-223, 1975.

[22] G. Gullberg, "The Attenuation Randon Transform: Theory and Application in Medicine and Biology". Ph.D. Thesis in Donner Lab. in UCBL., 1979.

[23] L. Chang, "A Method for Attenuation Correction in Radionuclide Computed Tomography". IEEE Trans. Nucl. Sci., vol.25, 638-643, 1978.

[24] C. Floyd, R. Jaszczak, K. Creer and R. Coleman, "Deconvolution of Compton Scattering in SPECT". J. Nucl. Med., vol.26, 403-408, 1985.

[25] J. Beck, R. Jaszczak, R. Coleman, et al, "Analysis of SPECT Including Scatter and Attenuation Using Sophisticated Monte Carlo Modeling Methods". IEEE Trans. Nucl. Sci., vol.29, 506-511, 1982.